

Propulsion Powertrain Component Modeling for an All-Electric Aircraft Mission

Saakar Byahut* and Alejandra Uranga†

University of Southern California, Los Angeles, CA 90089, USA

Electrification of the aircraft propulsion system has the potential to decrease the flight energy requirement, by leveraging higher component efficiencies as well as distributed propulsion and boundary layer ingestion. Previous results have shown an energy-usage benefit for small all-electric aircraft over conventional aircraft, but the benefit is highly sensitive to the underlying technology-level and modeling assumptions. This work presents models for the components of an all-electric propulsion system (battery, converter, motor) at a fidelity level that captures their operational behavior under the variable-power loads of the different flight segments. They are integrated into an all-electric propulsion powertrain sized for a commuter aircraft mission carrying 19 passengers over 100 nmi, as well as for the NASA X-57 Maxwell mission. Results using these higher-fidelity models predict a heavier propulsion system that consumes more energy than what is obtained from low-fidelity models with a constant-power, cruise-only representation of the mission. Motors and converters, sized for the maximum power requirements in a mission, show differences in efficiencies even across lower-power segments. Resulting system voltages are found to be well beyond currently certifiable limits. Distributed propulsion helps bring system voltages down with a small powertrain efficiency penalty, but increases the mass of the powertrain components.

I. Introduction

A. Motivation and Background

The steady growth in the demand for air transportation and the increasing emphasis on environmental sustainability in recent years have opened up the aircraft design space for novel architectures and configurations that could enable much higher energy efficiency levels for commercial aircraft. One promising avenue is the use of electrical components to generate the propulsive forces.

Electrification of the aircraft propulsion system can leverage higher component efficiencies, as well as enable additional benefits through distributed propulsion (DP) and boundary layer ingestion (BLI), to potentially provide energy usage benefits over current hydrocarbon-fueled aircraft. There are, however, inherent challenges with electrification. Batteries currently have almost two orders of magnitude smaller pack-level specific energies (energy per unit mass) at about 175 Wh/kg than hydrocarbon fuels' roughly 13 000 Wh/kg, and even with substantial improvements, are unlikely to reach specific energies comparable to fuel. Therefore, replacing an existing propulsion system with an electrified system is not expected to yield benefits due to the added complexity and weight [1]. Instead, the full aircraft has to be reconfigured, to take advantage of higher power delivery chain efficiency, as well as to leverage DP and BLI.

In previous work [2], we focused on exploring the design space with low-fidelity models and a cruise-only analysis of electrified aircraft across different missions (payload and range), different technology levels for electrical components, and aircraft configurations with and without DP and BLI. Those results showed that there can be energy-usage benefits for electrified aircraft across various missions, with the largest energy benefits seen for small aircraft flying short missions. An all-electric commuter (thin-haul) aircraft was found to be feasible and even beneficial with technology levels that are expected to be reached within the next decade or two. However, the high sensitivity of those results to electrical component technology levels (energy-to-mass and power-to-mass assumed values), as well as to the sizing constraints, indicates the need for higher-fidelity electrical component models that capture their behavior for the variable power conditions of the full flight profile.

*PhD Candidate, Department of Aerospace and Mechanical Engineering, AIAA Student Member

†Gabilan Assistant Professor, Department of Aerospace and Mechanical Engineering, 854 Downey Way RRB 218, auranga@usc.edu, AIAA Senior Member

B. Scope

Going beyond the trends and relative benefits of the various power system architectures and definitively concluding whether electrification makes sense for specific missions can only be done on the basis of low-uncertainty representations of the propulsion system components, in particular with regards to masses and efficiencies. In order to address this challenge, this paper presents models of electric propulsion powertrain components — namely battery, converter, and motor — which capture operational behavior associated with variable power loads across the different flight segments. The components are then integrated into an all-electric propulsion powertrain for a commuter aircraft mission, which is sized based on the energy and power demands for the flight. The results quantify the masses of the components and of the overall propulsion powertrain, as well as energy requirements. Comparison is made with low-fidelity modeling results, and the differences explained in terms of operational behavior.

C. Terminology

The term *all-electric* is used to refer to a propulsion system architecture where all the energy needed for propulsion is stored in batteries. An all-electric architecture consists of a power delivery chain from the batteries to one or more converters, each of which powers a motor that drives a propulsor (typically a fan). The mission considered here is that of a *commuter aircraft*, carrying a payload of 19 passengers over 100 nmi. The Viking Air Twin Otter is a representative commuter aircraft that serves as the conventional baseline for the analysis.

Low-fidelity modeling refers to the representation of the propulsion system components as being sized based on their energy or power requirement via assumed specific energy or specific power (*i.e.*, energy or power per unit mass) values, as done in previous work [2]. In addition, components also have prescribed efficiencies. The chosen values for specific energy, specific power, and efficiency are obtained from a review of current and future technology trends.

Higher-fidelity modeling refers to the approach used in the present work. These models capture operational behavior of the electrical components, such as the nonlinear discharge of a battery, or the variable efficiency of a motor running at variable power. They do not, however, attempt to account for the materials that make up these components, as the goal is to produce models that can be used interchangeably and reflect changes in technology levels rather than having to rely on material property libraries. These models still use specific energy and specific power values to size them, but present a more accurate picture of how power is consumed. Component efficiencies are calculated at different points of operation based on how efficiently power flows through the component for a certain power load or flight segment.

II. Component Models

At the system level, the propulsion system is characterized by its power, energy, and mass. The modeling goal is thus to predict values for these characteristics, in order for the propulsion system to then be integrated into an aircraft sizing and mission analysis framework. This work focuses on an all-electric propulsion powertrain, with a power chain of battery-converter(s)-motor(s) delivering power to propulsor fan(s). We model batteries, converters and motors (which put together we refer to as the *powertrain*), but leave out the propulsor fan for now. Distributed propulsion is represented by the number of fans driven electrically, with $N_{fanE} > 2$, where each fan is assumed to be driven by a converter-motor array. Boundary layer ingestion is left out for the aircraft-level framework in which our powertrain would be integrated.

A. Low-Fidelity Models

A basic representation of an electrified propulsion system is obtained by specifying values for each component's specific power, specific energy, and efficiency, more details of which are given in [2, 3]. These low-fidelity models assume a constant-power operation. While components are sized for the highest power needed over a mission, this approach assumes the components run at the same efficiency at those segments requiring less power than what they are sized for.

The battery, which acts as both an energy source and a power source, is characterized by its total available energy, E_{bat} , and the instantaneous power it supplies, P_{bat} . The Ragone relation [4] models the non-dimensional relationship between battery efficiency, η_{bat} , and power as

$$\frac{P_{bat}}{P_{max}} = 4 \eta_{bat} (1 - \eta_{bat}), \quad (1)$$

where P_{max} is the maximum power that the battery can deliver. The efficiency accounts for the losses inside the battery and models the fact that the usable amount of energy effectively decreases as the battery is operated at higher power.

Dividing E_{bat} and P_{max} by the battery mass results in battery specific energy (BSE) and battery specific power (BSP), both important technology parameters.

The converter and motor both convert power with a certain efficiency. Therefore, the relevant parameters used to model these two components are their respective powers, P_{conv} and P_{mot} , and efficiencies, η_{conv} and η_{mot} .

B. Higher-Fidelity Models

This paper presents a set of higher-fidelity models that capture operational behavior of components under different power loads, so the components can be sized accordingly. They are of higher-fidelity than the models in Sec. II.A, but without going into the detailed analyses of the properties of materials used to manufacture these components. The propulsion powertrain in Sec. III integrates these models in such a way that the components could be replaced with alternative or updated models.

1. Battery Model

Batteries have different discharge profiles based on a variety of factors, including electrical loads on the battery, cell chemistry, operating temperature, and age. Different batteries also use various forms of packaging, resulting in a knockdown from cell-level specific energy and power values to pack-level. While it is difficult to find detailed specifications for battery packs in commercial use, most packs consist of standard cells whose manufacturer specifications are generally available and can be used to build up a battery model.

We only model here the discharge of batteries, with the goal of assembling the simplest model of an all-electric powertrain that only depletes the battery through the mission. The charging behavior would be different than just the inverse of a discharge, and is left to be modeled in future work.

The nearly-linear discharge model of [5] is used here. It takes into account the nonlinear nature of discharge by performing a curve fit on discharge data from manufacturer cell specification sheets to obtain an equation for capacity discharge. Cell capacity, denoted Q , is the amount of available charge in units of Ampere-hours (Ah). A discharge curve plots the capacity against the voltage, V .

Figure 1 shows the discharge profile of the Samsung INR 18650-30Q cells used in the NASA X-57 Maxwell [6]. The voltage drop as the capacity decreases is nonlinear around the upper and lower extremes of capacity, and fairly linear in the middle. The different currents show how the capacity would discharge under different loads, with faster depletion at higher discharge currents.

It is important to note that the entire capacity of the cell cannot be used. Dipping into the upper extremes of capacity reduces the lifetime of the cells and degrades performance through faster discharging. Frequent charging to 100% capacity stresses the cells and thus also shortens battery life. Consequently, only the middle portion of the capacity is to be used in practice. For this analysis, it is therefore assumed that the lower 10% and upper 20% of the capacity are unavailable following [5].

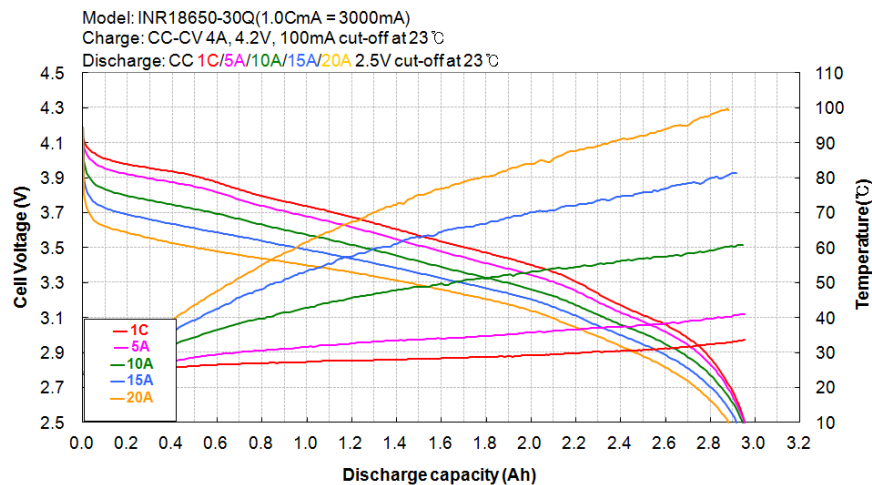


Fig. 1 Discharge profile of the cell used in the batteries of the all-electric NASA X-57 Maxwell [6].

Once we limit ourselves to the capacity range of 10% to 80%, the discharge curve is almost linear. A simple, nearly-linear equation [5] models this region of discharge as

$$V = V_0 - KQ - RI - GIQ, \quad (2)$$

where V is the voltage under the electrical current I , V_0 is the open source (no load) voltage that can be found in the cell datasheet, Q is the total capacity discharged up to the present instant in time, and R is internal resistance of the cell. The two modeling constants are K , which sets the primary dependency between voltage and capacity, and G , which represents the change in the slope of the discharge curve due to current.

Fitting the discharge model equation 2 to the manufacturer's discharge curves allows us to determine the four unknowns in the above equation: K , R , V_0 , and G . The values of K and G can be found from the slopes of two discharge lines (a system of two linear equations), while V_0 and R (if not given by the manufacturer) can be obtained from the y-intercepts. Using this approach, the parameters for the cells of the X-57 are found to be: $K=0.371$ V/Ah, $G=-0.00520$ V/A²h, $V_0=4.16$ V, and $R=0.0265$ Ω .

The above approach assumes constant current throughout discharges and only traverses one current curve at a time. However, for aircraft applications, the cell does not discharge at a constant current; instead, it discharges at (piecewise) constant power based on utilization along flight segments. Since power is the product of current and voltage for DC circuits, the previous equation can be rewritten in terms of power, P , as

$$V = V_0 - KQ - RP/V - GQP/V. \quad (3)$$

In order to easily compute the energy consumption, this expression is linearized as follows. Introduce the first-order Taylor series expansion of $1/V$ and Q/V about a point (Q_n, V_n) on the curve,

$$\frac{1}{V} \approx \frac{1}{V_n} - \frac{1}{V_n^2} (V - V_n), \quad (4)$$

$$\frac{Q}{V} \approx \frac{Q_n}{V_n} - \frac{Q_n}{V_n^2} (V - V_n) + \frac{1}{V_n} (Q - Q_n). \quad (5)$$

into Equation (3), and rearrange to solve for the voltage, thus obtaining the linear expression

$$V = V_n - \tilde{K} (Q - Q_n), \quad (6)$$

$$\text{where } \tilde{K} \equiv \frac{K + GP/V_n}{1 - RP/U_n^2 - GPQ_n/U_n^2}, \quad (7)$$

$$\text{and } V_n \equiv \frac{1}{2} \left[(V_0 - KQ_n) + \sqrt{(V_0 - KQ_n)^2 - 4(RP + GPQ_n)} \right]. \quad (8)$$

The energy ΔE provided during a discharge period is the integral of the voltage with respect to charge: $\Delta E = \int dE = \int V dQ$. This integral can be evaluated as the area of the trapezoid under the V vs. Q line, namely

$$\Delta E = \frac{1}{2} (V_i + V_f) (Q_f - Q_i), \quad (9)$$

in which (V_i, Q_i) and (V_f, Q_f) are the points at the start and end of the discharge, respectively. Substituting expressions for V_i and V_f from the linearized model in Equation (6) and simplifying yields the energy provided by the battery:

$$\Delta E = \left[V_n - \tilde{K} \left(\frac{Q_i + Q_f}{2} - Q_n \right) \right] (Q_f - Q_i). \quad (10)$$

In the above equation, the constant power appears explicitly in the expression (7) for \tilde{K} . Additionally, if the energy is thought of as the time integral of power, then the energy delivered over a short time Δt is simply the product $\Delta E = P \Delta t$.

While simple, this model captures the constant-power dynamics of battery cells, useful for modeling flight segments with different power requirements. The constant power energy delivery over small increments of time can be piecewise integrated to offer a picture of what the energy consumption would be over the entire mission while accounting for the effect of power level on energy consumption. Furthermore, this models allows analysis of cells that are already in the market. Novel battery cells can be incorporated via their discharge profiles, and one can then evaluate whether those cells could form building blocks of batteries to benefit powered aircraft.

2. Motor Model

The motor model is derived using a first-principles approach that considers the flux paths through the stator and rotor, including the stator/rotor poles and yokes, the air gap, and the rotor shaft. A *Switched Reluctance Motor* (SRM) is chosen for its suitability in high-speed as well as variable-speed operations [7] — needed to deliver the different power levels across different flight segments SRMs offer a high power density and a compact size. These motors offer high reliability as well, as the motor phases are electrically independent with negligible mutual coupling. As a result, even if one phase develops a fault, the motor can still operate, although at reduced power. In addition, SRM design is simpler since the machine has windings in the stator only, negating the complexity of having windings in the moving rotor. Having windings in the stator also allows for better manufacturability, greater accessibility in terms of maintenance, and easier cooling. The Boeing SUGAR Volt concept is an example of a study that opted for an SRM. [8]. Drawbacks include high torque ripple, which can be controlled with careful design, and acoustic noise, whose reduction is the topic of ongoing research [7].

An SRM, whose cross-section is schematically illustrated in Fig. 2, consists of an outer portion that houses the stator yoke and the stator poles, and an inner portion that includes the rotor poles, the rotor yoke, and the rotor shaft, with an air gap separating the two portions. The stator poles have windings (coils) around them, through which current flows to induce a magnetic field. In the position shown in Fig. 2, diametrically opposite rotor poles R_2 and R_2' are aligned with stator poles S_B and $S_{B'}$, respectively. When current flows in the windings around diametrically opposite stator poles (S_A and $S_{A'}$), the resulting magnetic field attracts the unaligned rotor pole pairs R_1 and R_1' towards S_A and $S_{A'}$, respectively. Once these rotor poles and stator poles are aligned, the current in the windings around stator poles S_A and $S_{A'}$ is turned off, and the current in the windings around stator poles S_B and $S_{B'}$ is turned on. This switching of current attracts R_1 and R_1' towards S_B and $S_{B'}$, respectively. If the current is switched in the sequence ABC the rotor rotates clockwise, whereas a sequence ACB produces a counterclockwise rotation. A q -phase SRM has a number N_{SP} of stator poles and a number N_{RP} of rotor poles in the ratio $q : q - 1$. The motor shown in Fig. 2 has 6 stator poles and 4 rotor poles, making it a 3-phase machine.

We adopt the method from [7] for sizing the SRM based on power output, which is as follows. When the rotor pole pairs are aligned or unaligned with the stator pole pairs, flux linkages are present because of the flux paths induced by the magnetic field. Flux linkage, λ , is defined as

$$\lambda = L(\theta, I) I, \quad (11)$$

where L is the inductance, θ is the rotor position, and I is the operating current. Figure 2 shows a representative flux linkage versus operating current plot for the aligned and the unaligned cases. The area between the aligned and unaligned curves represents the incremental mechanical work done per stroke, δW_m , of the machine operating at a peak current I_p . The average torque can then be calculated as

$$\mathcal{T}_{\text{avg}} = \frac{\delta W_m N_{SP} N_{RP}}{2\pi}. \quad (12)$$

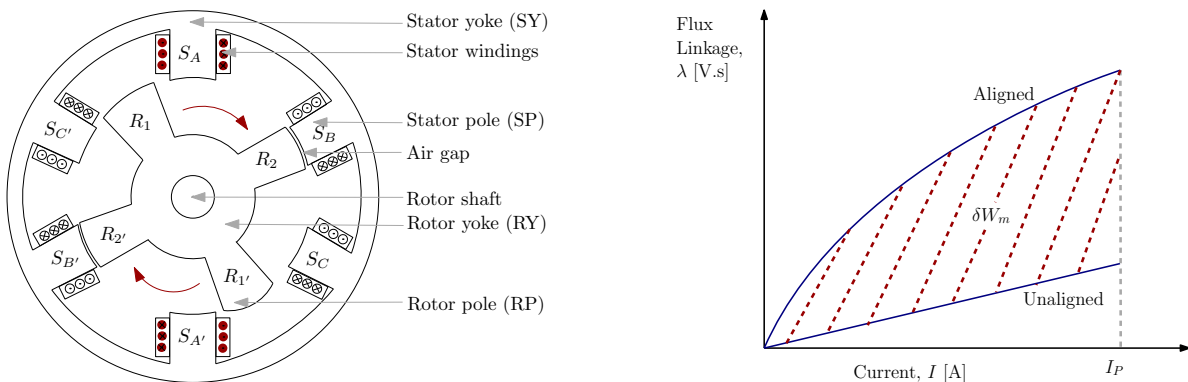


Fig. 2 (Left) Switched Reluctance Motor (SRM) cross-section schematic, and (right) illustration of flux linkages versus current curves for an SRM.

The mechanical power that the motor outputs is then the product of its average torque and the operating rotational speed,

$$P_{\text{out,mot}} = \mathcal{T}_{\text{avg}} \omega_{\text{mot}} . \quad (13)$$

Thus, calculating the output power of the motor involves generating the flux linkage plots for the aligned and unaligned cases, then calculating the area between them. Since the flux linkage λ is a product of the inductance L and the current I , it is sufficient to calculate the inductances for the aligned and unaligned cases.

The left side of Fig. 3 shows the flux paths when a rotor pole pair is aligned with a stator pole pair. The flux paths can be divided into two sub-paths: FP1, shown as blue dashed lines, and FP2, shown as solid red lines. Each sub-path is modeled differently. For the flux sub-path FP1, a magnetic equivalent circuit, as seen in Fig. 3, is constructed using all the segments of the motor that the flux passes through (stator yoke, stator poles, air gap, rotor poles, and rotor yoke). Each segment has an associated reluctance, analogous to a resistance in an electrical circuit. The magnetic flux, ϕ , through each segment is the ‘‘current’’, and the magnetomotive force (mmf), F , is analogous to the electromotive force.

By Ampere’s circuital equation, the applied mmf has to equal the sum of the mmf’s across each segment, such that

$$F_1 = \sum_{\text{paths}} H \ell = 2 (H_{\text{SP}_1} \ell_{\text{SP}_1} + H_{\text{RP}_1} \ell_{\text{RP}_1} + H_{\text{G}_1} \ell_{\text{G}_1}) + \frac{1}{2} (H_{\text{SY}_1} \ell_{\text{SY}_1} + H_{\text{RY}_1} \ell_{\text{RY}_1}) , \quad (14)$$

where H represents the magnetic field intensity and ℓ , the average length of the flux path in a segment. The subscripts SP and RP respectively indicate stator and rotor poles; the subscripts SY and RY respectively indicate stator and rotor yoke; and the subscript G refers to the air gap. The magnetic flux in the aligned scenario is the product of the magnetic flux density, B , and the area of the segment in the flux path, A . For the stator pole, it is then

$$\phi_a = B_{\text{SP}_1} A_{\text{SP}_1} , \quad (15)$$

with similar expressions for the remaining segments. To calculate the inductance and ultimately the output motor power, a flux density in the stator poles, B_{SP_1} , is assumed, and the flux densities in the other segments calculated per the corresponding area relative to that of the stator pole, namely

$$B_{\text{G}_1} = \frac{\phi_a}{A_{\text{G}_1}} = B_{\text{SP}_1} \left(\frac{A_{\text{SP}_1}}{A_{\text{G}_1}} \right) , \quad (16)$$

$$B_{\text{RY}_1} = \frac{\phi_a}{2A_{\text{RY}_1}} = \frac{B_{\text{SP}_1}}{2} \left(\frac{A_{\text{SP}_1}}{A_{\text{RY}_1}} \right) , \quad (17)$$

$$B_{\text{SY}_1} = \frac{\phi_a}{2A_{\text{SY}_1}} = \frac{B_{\text{SP}_1}}{2} \left(\frac{A_{\text{SP}_1}}{A_{\text{SY}_1}} \right) , \quad (18)$$

$$B_{\text{RP}_1} = \frac{\phi_a}{2A_{\text{RP}_1}} = \frac{B_{\text{SP}_1}}{2} \left(\frac{A_{\text{SP}_1}}{A_{\text{RP}_1}} \right) . \quad (19)$$

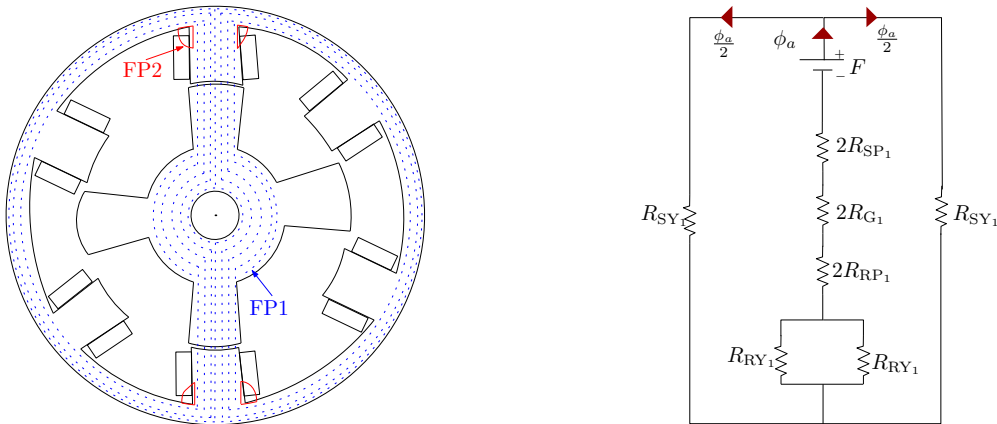


Fig. 3 (Left) Flux paths when the rotor and stator pole pairs are aligned, and (right) magnetic equivalent circuit for flux path FP1 (blue paths in the left image).

The mmf for each segment is then calculated by looking up the magnetic field intensity (H) values from a B - H curve of the lamination material. We assume in this work that the material is electrical-grade M19 steel [9]. The products $H \ell$ of different segments are summed up to obtain an estimate of F_1 . Since the applied mmf should be equal to

$$F_1 = (N_{\text{coil}}/q) I, \quad (20)$$

where (N_{coil}/q) is the number of turns of winding per phase and I the current through the motor, we iterate on the initial guess for B_{SP_1} until

$$\sum_{\text{paths}} H \ell = (N_{\text{coil}}/q) I. \quad (21)$$

With the converged values of the H 's, the reluctances for each segment can now be calculated as

$$R_{\text{SP}_1} = \frac{H_{\text{SP}_1} \ell_{\text{SP}_1}}{B_{\text{SP}_1} A_{\text{SP}_1}}, \quad (22)$$

$$R_{\text{G}_1} = \frac{\ell_{\text{G}_1}}{\mu_0 A_{\text{G}_1}}, \quad (23)$$

$$R_{\text{RP}_1} = \frac{H_{\text{RP}_1} \ell_{\text{RP}_1}}{B_{\text{RP}_1} A_{\text{RP}_1}}, \quad (24)$$

$$R_{\text{SY}_1} = \frac{H_{\text{SY}_1} \ell_{\text{SY}_1}}{B_{\text{SY}_1} A_{\text{SY}_1}}, \quad (25)$$

$$R_{\text{RY}_1} = \frac{H_{\text{RY}_1} \ell_{\text{RY}_1}}{B_{\text{RY}_1} A_{\text{RY}_1}}, \quad (26)$$

where μ_0 is the permeability of free space. Finally, the inductance can be computed as

$$L_{a_1} = \frac{(N_{\text{coil}}/q) \phi_a}{I} = \frac{(N_{\text{coil}}/q)^2}{R_{\text{EQ}_1}}, \quad (27)$$

where R_{EQ_1} is the total reluctance of the magnetic equivalent circuit, found by replacing the reluctance network in Fig. 3 by an equivalent reluctance, in a manner similar to how a resistor network is replaced by an equivalent resistor for electrical circuits.

A similar iterative procedure is used to calculate the inductance due to flux path FP2, which only includes the stator poles and the stator yoke. Only three-quarters of the stator mmf accounts for the flux in FP2, but there are four paths, so the inductance due to FP2 in the aligned case is

$$L_{a_2} = 4 \left(\frac{(N_{\text{coil}}/q) \frac{3}{4} \phi_a}{I} \right) = \frac{3 (N_{\text{coil}}/q)^2}{R_{\text{EQ}_2}}. \quad (28)$$

where R_{EQ_2} is the total reluctance of the magnetic equivalent circuit of FP2. The total aligned inductance is then the sum of the inductances due to the two parts

$$L_a = L_{a_1} + L_{a_2}. \quad (29)$$

The process for calculating the inductances for the unaligned case is more complex, since the flux paths do not flow as cleanly from the stator poles to the unaligned rotor poles. Instead, they break away from the stator poles at angles and enter rotor poles at angles, requiring the use of trigonometry to estimate average path lengths and segment areas covered. Instead of two flux sub-paths, the flux lines must be divided into more sub-paths, each requiring its own analysis of equivalent magnetic circuit, Ampere's law equation, *etc.* The iterative process of calculating the magnetic flux density for the unaligned case in each segment and thus the inductance is nevertheless similar to the aligned case. The method is described extensively in [7], and will not be reproduced here. Figure 4 presents this method as an algorithm.

After all the inductances are calculated, the process is repeated for a range of operating currents from low current to the peak current of the machine. The flux linkage ($\lambda = L I$) is then computed and plotted against current. The area between the aligned and unaligned flux linkage is used to calculate torque, and hence the output power.

The power output by the motor is smaller than the power that it receives due to the presence of losses in the system, which can be divided broadly into two types: copper losses, or losses in the windings around the stator field as current

flows through them; and core losses, or losses at the core parts of the motor which is typically made of a ferromagnetic material. Copper losses are due to the resistance of the wires making up the coil, and the power loss can be calculated as

$$P_{\text{Cu}} = q I^2 (R_{\text{coil}}/q), \quad (30)$$

where q is the number of phases in the motor, I is the operating current, and (R_{coil}/q) is the resistance of the stator winding per phase. This resistance can be calculated using the standard equation for the resistance of a wire,

$$(R_{\text{coil}}/q) = \frac{\bar{\ell}_{\text{coil}} (N_{\text{coil}}/q)}{\sigma A_{\text{coil}}}, \quad (31)$$

where σ is the specific conductivity of the conductor (usually copper), $\bar{\ell}_{\text{coil}}$ is the mean length of wire in one turn of the coil, (N_{coil}/q) is the number of turns per phase, and A_{coil} is the cross-sectional area of the conductor.

Core losses are determined using power loss coefficients tabulated according to the motor switching frequency and operating speed. Core losses can be subdivided into three types: hysteresis, eddy-current, and excess losses. Hysteresis losses arise from changes in the flux density B and magnetic field intensity H of the core. Eddy-current losses are due to parasitic currents through the core. Excess losses are produced by the movement of the magnetic domain walls, as

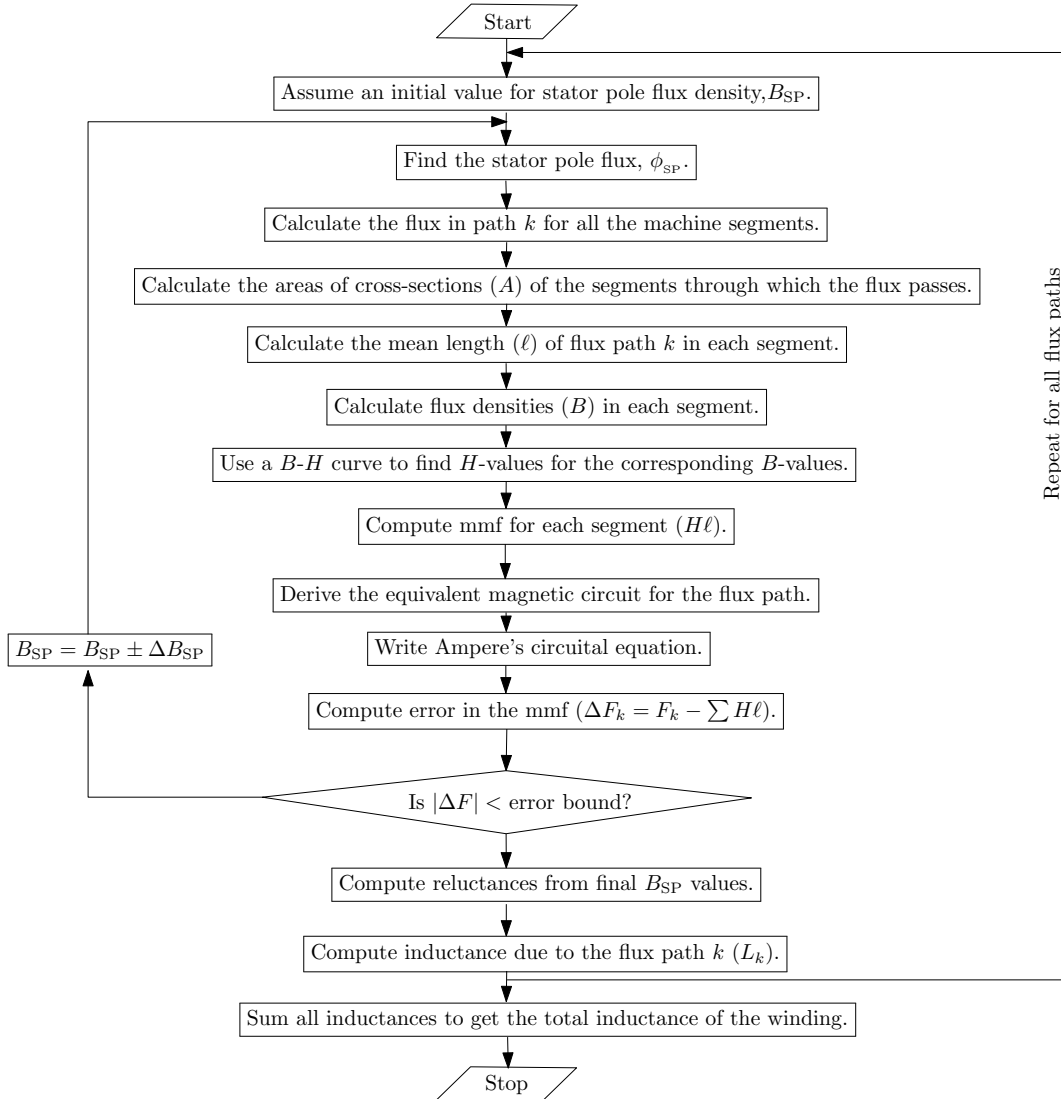


Fig. 4 Algorithm to calculate inductances for the motor (adapted from [7]).

Table 1 Motor core power loss coefficients for the different motor segments and loss types.

Segment	Core Loss Coefficients [W/kg]		
	Hysteresis \mathcal{P}_{hys}	Eddy-current $\mathcal{P}_{\text{eddy}}$	Excess \mathcal{P}_{exs}
Stator pole	5	13	1.4
Rotor pole	8	32	1.8
Stator yoke	3.5	19	0.95
Rotor yoke	9.5	20	1.3

well as the rotation of the domain dampened by eddy currents [10]. For a switched-reluctance motor operating across a range of speeds, specific power loss coefficients \mathcal{P} (power lost per unit mass) were calculated for each segment (stator yoke, stator poles, rotor yoke, and rotor poles) and for each core loss type in [10]. The results revealed that the loss coefficients are relatively insensitive to operating speed. Therefore, for this analysis, loss coefficients are assumed to be constant and given the values in Table 1.

The total core losses are then calculated as a sum of the core losses of all segments

$$P_{\text{core}} = \sum_k \mathcal{P}_k m_k = \sum_k (\mathcal{P}_{\text{hys},k} + \mathcal{P}_{\text{eddy},k} + \mathcal{P}_{\text{exs},k}) \rho_k \mathcal{V}_k, \quad (32)$$

where ρ_k , m_k , \mathcal{V}_k are the density, total mass, and total volume of segment k respectively. That is, for N_{RP} rotor poles, m_{RP} includes the mass of all of them.

The input power to the motor is then the sum of the output power and the losses

$$P_{\text{mot,in}} = P_{\text{mot,out}} + P_{\text{Cu}} + P_{\text{core}}, \quad (33)$$

and the motor efficiency is given by

$$\eta_{\text{mot}} = \frac{P_{\text{mot,out}}}{P_{\text{mot,in}}}. \quad (34)$$

3. Converter Model

A switched reluctance motor (SRM) requires a converter to switch power delivery among its phases. Over one switching cycle, each phase of the motor needs to have the associated windings energized so that the rotor poles align with them sequentially, and the motor completes revolutions to generate mechanical energy. SRMs run on DC power since the switching of current (turning current on and off) sequentially between the phases is enough to drive the motor. The appropriate converter can then be modeled as a non-ideal DC-DC transformer, or equivalently, an ideal DC-DC transformer plus losses [11].

The ideal converter, illustrated in Fig. 5(a), is represented as the DC-DC transformer equivalent circuit of Fig. 5(b). The output voltage $V_{\text{conv,out}}$, resistance R_{load} , and current I represent the connection to the motor, while the input represents the power delivered by the battery. A control input called the duty cycle, k_d , determines what fraction of the cycle has current on and what fraction has current off out of the cycle length (period) τ . The duty cycle changes based on the switching requirements of the motor. The current time-evolution through the circuit, illustrated in 5(c), has a peak value I_P with ripples of magnitude Δi assumed small compared to I_P . The model shows an error of about 0.3% for $\Delta i/I_P = 0.1$, so the DC transformer approach works well to represent the converter [11]. The output voltage, $V_{\text{conv,out}}$, is a function of the input voltage, $V_{\text{conv,in}}$, and we need to construct a model for their relationship.

The non-ideal or practical converter, shown in Fig. 6, consists of switches and diodes, which have an associated resistance and a voltage drop when in operation that make up the switching losses. The resistance of the wiring is also taken into account, and results in copper losses similar to those of the motor. When the current is high ($I = I_P \pm \Delta i$ from $t = 0$ to $t = k_d \tau$), the switch is on and the diode is reverse-biased, leading to an open circuit where the diode is located. Using Kirchoff's voltage and current laws (KVL and KCL), we can write expressions for the voltage drop across the

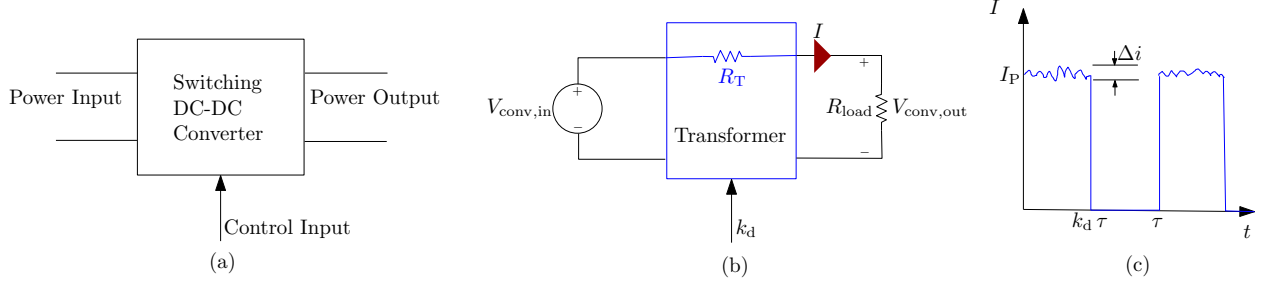


Fig. 5 Schematic of (a) ideal DC-DC converter, (b) equivalent circuit for DC-DC transformer representation of the converter, and (c) current waveforms over a cycle.

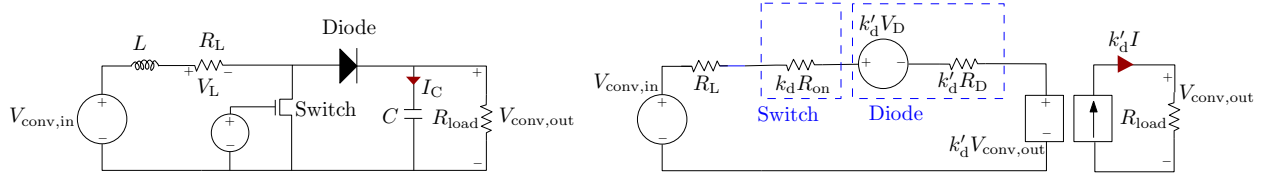


Fig. 6 Non-ideal converter: (left) schematic with switch, diode, and inductance, and (right) equivalent circuit model for a full cycle of operation.

inductor and for the current through the capacitor respectively as

$$\text{for } 0 \leq t \leq k_d \tau, \quad V_L(t) = V_{\text{conv,in}} - I R_L - I R_{\text{on}} \quad (35)$$

$$\text{and } I_C(t) = -\frac{V_{\text{conv,out}}}{R_{\text{load}}}, \quad (36)$$

where R_L is the resistance of the inductor and R_{on} is the on-resistance of the switch. When the current is low, the switch turns off, but the diode is forward biased by the inductor current. Using KVL and KCL again for this case gives

$$\text{for } k_d \tau \leq t \leq \tau, \quad V_L(t) = V_{\text{conv,in}} - I R_L - V_D - I R_D - V_{\text{out}}, \quad (37)$$

$$\text{and } I_C(t) = I - \frac{V_{\text{conv,out}}}{R_{\text{load}}}. \quad (38)$$

The average of these over one time period, τ , are calculated as

$$\langle V_L \rangle = \frac{1}{\tau} \int_0^{\tau} V_L(t) dt, \quad (39)$$

$$\langle I_C \rangle = \frac{1}{\tau} \int_0^{\tau} I_C(t) dt. \quad (40)$$

Setting both these average voltage and current to zero allows us to determine the output voltage

$$V_{\text{conv,out}} = \frac{1}{k'_d} (V_{\text{conv,in}} - k'_d V_D) \left[\frac{k_d'^2 R_{\text{load}}}{k_d'^2 R_{\text{load}} + R_L + k_d R_{\text{on}} + k'_d R_D} \right], \quad (41)$$

which is a function of the duty cycle k_d , its complement $k'_d = 1 - k_d$, the input voltage $V_{\text{conv,in}}$, the voltage drop V_D across the diode, as well as the respective resistances R_{on} , R_D and R_L of the switch-on, diode, and inductor. It also depends on what the load is, in this case a motor with resistance R_{load} through which a current I flows.

We now have all the variables needed to calculate the input and output powers for the converter,

$$P_{\text{conv,in}} = V_{\text{conv,in}} I, \quad (42)$$

$$P_{\text{conv,out}} = V_{\text{conv,out}} k'_d I, \quad (43)$$

as well as the converter efficiency

$$\eta_{\text{conv}} = \frac{P_{\text{conv},\text{out}}}{P_{\text{conv},\text{in}}} . \quad (44)$$

For the subsequent analysis, we use the representative values for the on-resistance of diodes, $R_D = 0.5 \Omega$, the voltage drop across diodes, $V_D = 3.75 \text{ V}$, from [12], and the value on-resistance of switches, $R_{\text{on}} = 5 \Omega$ from [13]. The resistance of the inductor, R_L , is assumed to be negligible. All of these sub-components are assumed to be able to operate in high-voltage, high-current environments, as required for the large amounts of power consumed over aircraft flight.

III. Integration and Component Sizing

A. Propulsion Powertrain Integration

The all-electric propulsion system, illustrated in Fig. 7, consists of the power delivery chain starting at the battery, connected to a set of converters, each driving a motor that powers a propulsor fan. With N_{fan} propulsors and a propulsor efficiency η_{fan} , the total mechanical flow power added to the flow by the propulsion system is

$$P_K = N_{\text{fan}} \eta_{\text{fan}} P_{\text{shaft}} , \quad (45)$$

where P_{shaft} is the power delivered to each fan by its driving motor. In this work, the modeling control volume is drawn at the level of the powertrain (*i.e.*, battery + converters + motors) shown as the dotted line in Fig. 7, and we assume a constant propulsor fan efficiency $\eta_{\text{fan}} = 0.8$ following [2].

Each propulsor is powered by a motor, which delivers its power

$$P_{\text{shaft}} = P_{\text{mot},\text{out}} = \eta_{\text{mot}} P_{\text{mot},\text{in}} , \quad (46)$$

where η_{mot} is the efficiency of the motor. Similarly, each motor is driven by a converter, with all the converters powered by the battery, such that

$$P_{\text{mot},\text{in}} = P_{\text{conv},\text{out}} = \eta_{\text{conv}} P_{\text{conv},\text{in}} , \quad (47)$$

$$P_{\text{bat}} = N_{\text{fan}} P_{\text{conv},\text{in}} . \quad (48)$$

The mass of the propulsion powertrain is calculated by adding the masses of its components,

$$m_{\text{power}} = m_{\text{bat}} + N_{\text{fan}} (m_{\text{conv}} + m_{\text{mot}}) , \quad (49)$$

and the component masses are calculated from their specific energy or specific power

$$m_{\text{bat}} = E_{\text{bat}} / BSE \quad (50)$$

$$m_{\text{conv}} = P_{\text{conv},\text{in}} / SP_{\text{conv}} \quad (51)$$

$$m_{\text{mot}} = P_{\text{mot},\text{in}} / SP_{\text{mot}} . \quad (52)$$

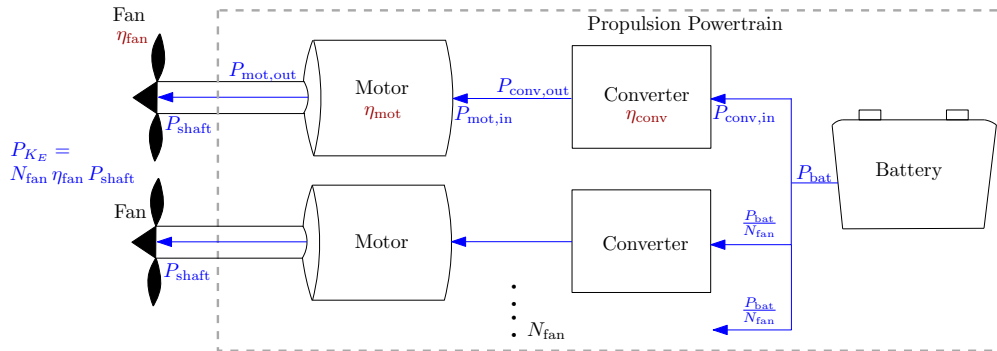


Fig. 7 Propulsion powertrain schematic.

Note that the propulsion powertrain used for mass calculation ends at the motor, and the mass of the propulsors is not included. Future work will also size the propulsors, and thus be able to account for the potential weight savings of distributed propulsion.

B. Component Sizing

The input to our powertrain model is the mechanical flow power profile, P_{KE} , along the various flight segments. These flow power requirements set the power input for each fan, P_{fan} , and the motors can be sized to supply that corresponding power ($P_{mot,out} = P_{fan}$). The converters in turn are sized to drive the motors ($P_{conv,out} = P_{mot,in}$), and converter efficiency dictates the amount of power that the full set of N_{fan} converter + motor elements draws from the batteries ($N_{fan} P_{conv,in} = P_{bat}$).

The battery acts as both a power and an energy source, the battery is sized to provide the energy required for the full mission while also being able to supply the power needed for each segment. The converter and motor only deal with power, and therefore their sizes are set by the maximum power that they have to supply over the mission. For example, if the climb segment requires the most power, then the converter and motor are sized for climb. For the rest of the segments, those same converter and motor are used, and the model thus captures the effect of the efficiency change in sub-maximum-power operation.

1. Motor

Motor sizing is based on the output equation for an SRM [7],

$$P_{out,mot} = \eta_{mot} k_d k_1 k_2 B A_s D^2 L \omega_{mot} , \quad (53)$$

where $k_1 \equiv \pi/4$, B is the motor's magnetic flux density, D its bore diameter (or the inner stator diameter), L its length in the direction perpendicular to the plane of the cross-section shown in Fig. 2, and ω_{mot} its rotational speed. Note that D is the diameter of the machine when the rotor is taken out and all that is left is the stator yoke and the stator poles with windings. As such, D incorporates the air gap ℓ_G between the stator poles and rotor poles in the aligned position.

To size the motor, it is common design practice to express its length as a fraction of the diameter, namely $L = k D$, such that the output equation becomes

$$P_{out,mot} = \eta_{mot} k k_d k_1 k_2 B A_s D^3 \omega_{mot} . \quad (54)$$

This expresses the output power as a function of the rotor bore diameter: $P_{out,mot} \propto D^3$, and provides a starting point to size the motor.

The duty cycle

$$k_d = \frac{\theta_i q N_{RP}}{2\pi}$$

is the fraction of a time period over which the current in a phase is high, and is calculated from the number of phases, q , the number of rotor poles, N_{motR} , and the current conduction angle for a rising induction profile

$$\theta_i = \frac{1}{2} [\theta_{RP} - (\beta_s + \beta_r)] ,$$

where

$$\theta_{RP} = \frac{2\pi}{N_{motR}}$$

is the rotor pole pitch (in radians), and β_s and β_r are the stator and rotor pole arcs respectively (also in radians).

The constant k_2 is determined by the unaligned inductance L_u and the slope L_a^s of the line joining the aligned inductance L_a to the origin in the flux linkage versus current plot of Fig. 2, as

$$k_2 = 1 - \frac{L_u}{L_a^s}$$

Finally,

$$A_s = \frac{2(N_{coils}/q) I m}{\pi D} .$$

Table 2 Technology scenarios: assumptions values for electrical component parameters.

Parameter	Current State-of-the-Art	Conservative 2035	Expected 2035	Optimistic 2035
Pack BSE [W·h/kg]	175	250	575	900
Motor Specific Power [kW/kg]	2	9	12	16
Converter Specific Power [kW/kg]	2.2	9	14	19

is the specific electric loading, calculated using the number of turns per phase N_{coils}/q , the current I , and the number of phases that conduct simultaneously m .

Initial values are assumed for all the constants that depend on the motor dimensions themselves, and the diameter is calculated for the required output power. Some of the motor dimensions have to be determined *a priori*, so parameters like phase, number of rotor and stator poles, have to be set first. This analysis assumes a 3-phase motor with 6 stator poles and 4 rotor poles, so we take $q=3$, $N_{\text{SP}}=6$, $N_{\text{RP}}=4$, and $m=1$.

These parameters in turn allow either calculations or setting limits on other geometric dimensions like β_s , β_r , and θ_{RP} . The rest of the dimensions are calculated using the geometry of the switched reluctance motor. An air gap length $\ell_G=0.5$ mm is assumed, in line with currently available industrial motors [7].

Through initial guesses of some parameters and calculations of others, the motor performance is analyzed using the model presented in Sec. II.B.2. The motor output power developed by the initial design is then checked against the required output power before iteratively re-designing the motor until the requirement is met. Once the design closes, the total input power to the motor, $P_{\text{mot,in}}$, is calculated by adding the output power and the losses. This motor input power becomes the output power for the converter ($P_{\text{conv,out}} = P_{\text{mot,in}}$), and provides the starting point for converter sizing.

2. Converter

The converter model takes the power required for the motor, the duty cycle, and the resistance of the motor windings as inputs, then sizes the converter based on the model for a DC-DC transformer with losses model of Sec. II.B.3. The converter losses (copper losses and switching losses) are calculated, and the sizing input power to the converter $P_{\text{conv,in}}$ for that flight segment determined, thus serving in turn to size the battery.

3. Battery

The power needed by the converter is multiplied by the number of propulsors to obtain the required power output of the battery: $P_{\text{bat}} = N_{\text{fan}} P_{\text{conv,in}}$. The model uses the method described in Sec. II.B.1 to size the battery for this power requirement. The power required is multiplied by the time duration for the flight segment to obtain the energy use by each segment, and the battery is sized to meet both the total mission energy consumption E_{bat} (sum of energy usages for all segments), and the power requirements of all segments.

C. Technology Scenarios

Table 2 summarizes the technology scenarios that are used in the present work to assess the effect of technology level on the feasibility of electrified aircraft. Only a general justification for the selected value is presented here, but the interested reader can find a detailed discussion behind the rationale for using these values in previous works [2, 3].

The current battery specific energy (BSE) was taken from the all-electric two-seater Airbus E-Fan [14]. Conservative 2035 BSE assumes no new breakthroughs in battery technology, whereas the optimistic value assumes novel battery chemistries that are made rechargeable and commercialized by that time. Expected 2035 are values in-between conservative and optimistic estimates.

For the other electrical components, the current and conservative specific powers and efficiencies are taken from a National Academies of Engineering report [15] on reducing global carbon emissions. Ongoing NASA-funded research has demonstrated much higher numbers at test-bed level [16], and it is reasonable to expect that these numbers may be achieved at the system level in 2035. Therefore, these numbers form the basis of the optimistic 2035 assumptions. All the expected 2035 assumptions are simply the average of the conservative and optimistic 2035 assumptions.

D. Aircraft and Mission Power Profiles

Since it is expected that all-electric power system architectures will only be feasible for small aircraft flying short missions in the near future, we study a commuter aircraft (modeled similarly to the Viking Air Twin Otter) and the all-electric NASA X-57 Maxwell, with the relevant mission parameters for both of these given in Table 3. The data was used to construct a mission power profile for the Twin Otter, while for the X-57 we use the representative power profile available through NASA. (thus the corresponding parameters in the table are only a reference).

Table 3 Baseline aircraft and mission specifications [17, 18]

		Twin Otter	X-57 Maxwell
Number of passengers	N_{pax}	19	3
Payload	m_{pay}	1 842 kg (3 979 lb)	–
Mission range	R	100 nmi (185 km)	100 nmi (185 km)
Cruise speed	V_{cruise}	94 m/s	77m/s
Takeoff mass	m_{init}	5 670 kg	1 400 kg
Cruise lift-to-drag ratio	$(L/D)_{\text{cruise}}$	12	–
Cruise altitude	h_{cruise}	10 000 ft (3 050 m)	8 000 ft (2 440 m)
Max rate of climb	\dot{h}_{max}	490 m/min	–
Climb gradient	dh/dR	107 m/km	–

1. Twin Otter Climb-Cruise-Approach Mission

For this mission profile, it is assumed that the Twin Otter climbs at constant power to reach its cruise altitude at the maximum climb rate and climb gradient. For approach, the descent rate is set to be half the magnitude of climb rate, while the descent gradient is fixed at the allowed maximum of 3° for an instrument landing system (ILS) approach. The remaining distance to be covered during the mission is assumed to be at cruise. What follows presents the method for determining the actual power profile.

The aircraft is assumed to climb continuously at constant power to reach its cruising altitude from sea level. Since the acceleration is assumed to be zero, the equations of motion for the aircraft are [19]

$$T_{\text{climb}} - D_{\text{climb}} - W \sin(\gamma) = 0 \quad (55)$$

$$L_{\text{climb}} - W \cos(\gamma) = 0, \quad (56)$$

where T_{climb} , D_{climb} , L_{climb} , and W are the four forces – thrust, drag, lift, and weight – on the aircraft during climb, and $\gamma = \arctan(dh/dR)$ is the climb angle set by the height-to-range climb gradient dh/dR . For all-electric aircraft, no fuel is burned and the weight is constant throughout the mission. Drag can be expressed as a function of lift using a reduced lift-to-drag ratio, in this case assumed to be $2/3$ of the cruise L/D ,

$$D_{\text{climb}} = \frac{L_{\text{climb}}}{(L/D)_{\text{climb}}} = \frac{L_{\text{climb}}}{\frac{2}{3}(L/D)_{\text{cruise}}} = \frac{W \cos(\gamma)}{\frac{2}{3}(L/D)_{\text{cruise}}}. \quad (57)$$

The climb speed can be estimated using the climb rate \dot{h} and the climb angle as

$$V_{\text{climb}} = \dot{h} / \sin(\gamma). \quad (58)$$

Then, the power required to climb is

$$P_{\text{climb}} = T_{\text{climb}} V_{\text{climb}}. \quad (59)$$

The time it takes to climb up to cruise level is determined by the cruise altitude and the rate of climb, while the energy consumed during climb is then the product of the climb power and climb time.

For cruise, lift balances weight and thrust balances drag, and thus thrust can be calculated as

$$T_{\text{cruise}} = D_{\text{cruise}} = \frac{L_{\text{cruise}}}{(L/D)_{\text{cruise}}} = \frac{W}{(L/D)_{\text{cruise}}}. \quad (60)$$

The cruise power and energy usage are then set by the cruise speed, V_{cruise} , and cruise time duration t_{cruise} , namely

$$P_{\text{cruise}} = T_{\text{cruise}} V_{\text{cruise}} \quad (61)$$

$$E_{\text{cruise}} = P_{\text{cruise}} t_{\text{cruise}} \quad (62)$$

Note that the cruising time is equal to the cruise range divided by cruise speed, both of which are mission parameters.

The approach segment is similar to the climb, except that the weight contribution in the thrust/drag/weight balance Equation (55) has the same sign as thrust since the angle γ is negative indicating a decent. We set the approach angle to $\gamma = -3^\circ$ per the standard ILS approach. The thrust and power requirement for descent is then of course lower than for climbing. In addition, we use the cruise lift-to-drag value for descent, such that

$$D_{\text{approach}} = \frac{L_{\text{approach}}}{(L/D)_{\text{approach}}} = \frac{L_{\text{approach}}}{(L/D)_{\text{cruise}}} = \frac{W \cos(\gamma)}{(L/D)_{\text{cruise}}} \quad (63)$$

Figure 8 shows the altitude and power profile for our representative climb-cruise-approach mission. These power values are used to simulate and size the propulsion system components for the commuter aircraft mission. The power needed for climb is over double that for cruise, whereas approach requires very little power.

2. NASA X-57 Maxwell Mission

Figure 9 gives the power profile of an X-57 Maxwell mission, including the takeoff, climb/cruise, and approach. The Maxwell flies a shorter mission than the Twin Otter, so its climb and cruise are modeled as one segment. This amounts to a continuous climb before descent. Takeoff is the highest-power segment and contributing to a large proportion of the mission time compared to the Twin Otter. For simplicity, the segments in the mission with zero power are not represented here, and taxiing before takeoff and after landing is also omitted.

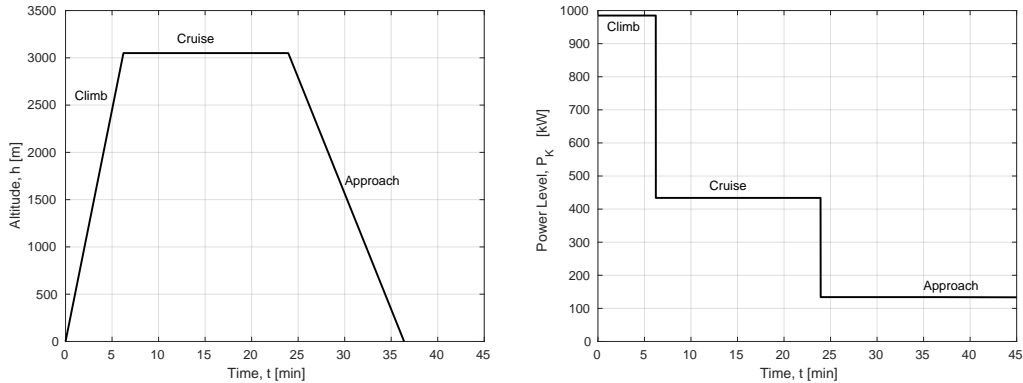


Fig. 8 Twin-Otter climb-cruise-approach mission: (left) altitude and (right) power profile.

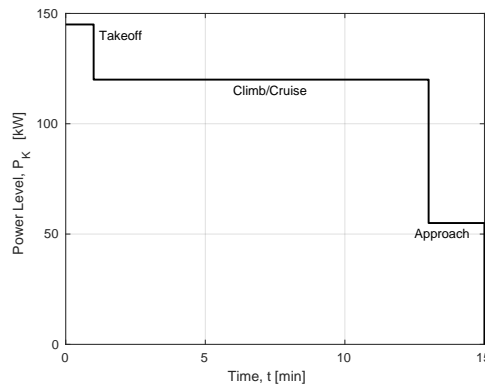


Fig. 9 Power profile of a NASA X-57 Maxwell flight (generated using data from [20]).

IV. Results

The all-electric propulsion powertrains constructed using the low-fidelity and higher-fidelity component models from Section II are simulated using the Twin Otter mission power profile from the previous subsection. The mass of the battery and the energy required are calculated using the two approaches of different fidelity and compared. Components are modeled with the Expected 2035 technology parameters from Section III.C. The efficiencies of each component at different flight segments is also analyzed for the Twin Otter and the X-57 Maxwell mission profiles. Voltage and current trends in the electrical system are considered. Finally, the effect of distributed propulsion (DP) on the efficiency as well as the mass of the propulsion powertrain is examined — though this does not include the sizing of the propulsor fans, so does not account for some of the weight saving benefits that DP could provide.

A. Comparison of Low- and Higher-Fidelity Models

Figure 10 shows the mass of the battery and the energy required for each flight segment, as well as the entire mission, for the Twin Otter. Note that in both low- and higher-fidelity models the battery is assumed to only operate between 10% and 80% charge level, as explained in Section II.B.1.

The biggest difference between the results predicted by the two fidelity levels is in the climb segment, for which the high-fidelity approach predicts 36% more energy usage. With the low-fidelity model, climb amounts to 40% of the total mission energy, while climb consumes 50% of the mission energy when using the higher-fidelity models. The energy consumed during approach is almost unaffected by the fidelity of the model due to the low-power level (and hence close-to-optimal battery operation). Because the higher-fidelity model predicts a larger battery, its cruise power draw is at a higher efficiency than that for a smaller battery, and the higher-fidelity model results in a 16% lower cruise energy consumption than the low-fidelity one. In terms of the overall mission, the higher-fidelity approach results in roughly 7% higher energy consumption than the low-fidelity model value.

This discrepancy between model fidelity levels is the result of the difference in battery discharge operation modeling, and its effects on predicted energy usage and battery mass. The motor and converter masses for each fidelity level are within 1% of each other, with the higher-fidelity model predicting slightly larger masses. However, the low-fidelity model does not capture the high-power battery discharge dynamics, while the higher-fidelity model does account for the loss in battery efficiency for high-power demands and hence predicts the need for a larger battery as a result. This distinction reveals the importance of accounting for the effect of power level on energy consumption at the battery level (basically the Ragone relation), and its impact on mission energy efficiency.

Another way to understand this, is that because of the dynamics of battery discharge, it is more constraining to require a very high power level during a short time, than it is to require a lower power level but for a longer time. As a result, the battery ends up being sized mostly to meet the demands of the climb segment.

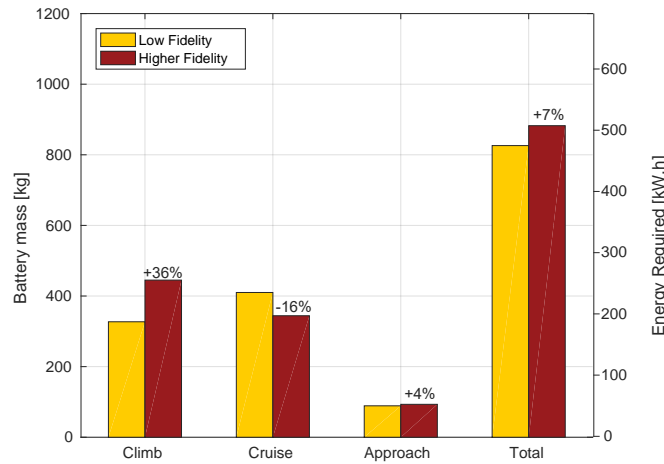


Fig. 10 Battery mass and energy differences for the low- and higher-fidelity models for the Twin Otter mission.

B. Component Efficiencies

Figure 11 shows the efficiency of the motors and the converters across the different flight segments. Both components are sized for the maximum power load they have to deal with, which occurs during climb for the Twin Otter mission and during takeoff for the Maxwell. The graphs show that the motor operates most efficiently at its design point (max power) in both cases. The efficiency drops in off-design cases such as approach, where the same motors sized for substantially higher power are running at lower power.

The motor losses account for these changes in efficiency. Core losses scale with motor weight, and since running the motor at lower power does not change its weight, the core losses stay relatively constant in absolute terms, but in relative terms the lost power is proportionally higher for low power-output operation. Winding (copper) losses scale with motor power: copper losses are lower at low power, but not low enough to offset the higher proportion of core losses. The overall effect is a drop in motor efficiency at lower powers. It should be noted that the motor efficiency never drops below 80% in both cases, meaning that an electric powertrain may well have an overall efficiency advantage over conventional system even if running at sub-optimal electrical component efficiencies.

The efficiency also drops more substantially for the Twin Otter mission than for the X-57 Maxwell. The Twin Otter is a bigger commuter aircraft and has two propulsors, while the smaller Maxwell has 14 distributed propulsors and a smaller payload. These differences affect the motor efficiency in two ways. First, the smaller Maxwell has a lower peak power demand than the Twin Otter. Second, the already smaller power demand is spread over 14 converter-motor-propulsor arrays. Therefore, the Maxwell's motors are substantially smaller than those on the Twin Otter.

The converter efficiency, on the other hand, behaves opposite to the motor efficiency. The switching losses are assumed to be constant, since the diodes and the transistor switches have the same on-resistance and voltage drop over a wide range of voltages [12, 13]. These make up a smaller portion of the converter losses, and even more so at high power, where the copper losses dominate. As a result, at high power, the converter efficiency drops due to higher copper losses, but improves at lower power.

C. Current and Voltage Considerations

All of the analyses in the previous subsections were run assuming a maximum current limit of $I_{\max} = 25$ A while letting voltage float. If we also impose a voltage limit of $V_{\max} = 540$ Vdc = ± 270 V to match the voltage level in today's Boeing 787 today [15], then the components cannot be sized for the power levels of a Twin Otter mission.

Without a maximum voltage constraint, the maximum system voltage reaches about 50 kV for the Twin Otter. This voltage is about two orders of magnitude larger than the limit imposed by Paschen's law (327 V above which electric arcing occurs between two closely spaced conductors), and comparable to voltages in ground-based power transmission lines. While there exist semiconductor components (transistors and diodes in the converter) capable of having breakdown voltages higher than this, the rest of the system needs to be able to handle the voltage as well. This necessitates the

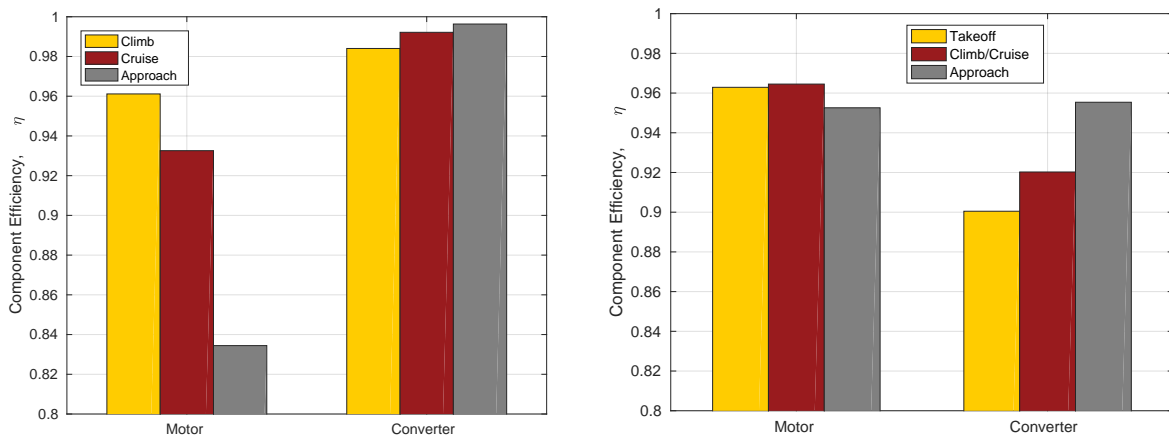


Fig. 11 Efficiency of motor and converter over the flight segments of the two missions considered: (left) Twin Otter and (right) X-57 Maxwell.

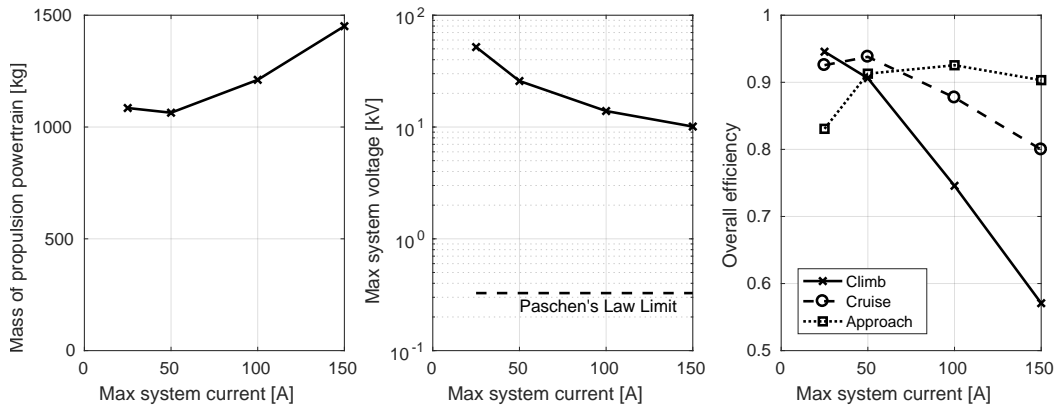


Fig. 12 Effects of changing current limit for Twin-Otter mission.

development of high-voltage distribution systems and a rethinking of the powertrain components. Specifically, the space between the windings in the stator inside the motor needs to increase, among other protective and operational changes.

Alternatively, or in addition, the current limit can be raised to bring system voltages down, since what needs to be met is a power (voltage times current) requirement. Figure 12 shows the effects of increasing the current limit for the Twin Otter mission profile. The mass of the propulsion system decreases first, but then starts to increase sharply beyond a maximum current of about 50 A. This is because the motor + converter efficiency first increases due to the copper losses (proportional to the square of current) still being smaller than the core losses for the motor and switching losses for the converter. When the current increases further however, the copper losses start to dominate, bringing the efficiency down and requiring a larger battery to compensate for the increased losses, which results in a less efficient and heavier propulsion powertrain. The maximum system voltage does drop to about 10 kV for $I_{\max} = 100$ A, but this value is still more than an order of magnitude larger than the Paschen's law limit.

Note that we could not find B - H curves (needed to get magnetic field intensity values from magnetic flux density for the motor model) that go up to the high B -values associated with currents larger than $I_{\max} = 150$ A, and we therefore did not try currents above this limit.

The conclusion of these current-versus-voltage trade-off considerations is that high-voltage, high-current distribution systems and propulsion components need to be developed in order to enable the use of an all-electric powertrain even for commuter aircraft.

D. Distributed Propulsion (DP)

Distributed propulsion has the potential to decrease propulsion system mass due to the cube-squared relationship between thrust (which scales with propulsor area, and hence length squared) and propulsion weight (which scales with volume, and hence length cubed). Most of the weight changes would be in the fans and nacelles, which we do not model here, but we can look at the effect of distribution on the powertrain mass and efficiency, as well as on maximum voltage.

Figure 13 shows the effect of increasing the number of propulsors on the propulsion powertrain. As the number of propulsors goes up from 2 to 20, the mass of the powertrain increases slightly, while the maximum system voltage considerably drops from around 50 kV to 5 kV — though still an order of magnitude higher than the Paschen's law limit. Overall, distributed propulsion shows the same effects as that of raising the current limit in the previous section: advantage up to a point, then efficiencies start to drop and masses to increase as copper losses become dominant.

A definite advantage of distribution is the reduction by an order of magnitude of the system voltage. In conjunction with higher currents, the system volume may be lowered further, reducing the need for high-voltage, high-current distribution systems and components.

While the results shown here do not readily encourage the use of distribution in the propulsive powertrain, this analysis only presents the worst aspects of distribution, namely the motor and converter efficiency drops. The drop in powertrain efficiency with distribution is nevertheless small, and the resulting powertrain mass gain is thus unlikely to offset the mass reductions that the cube-squared weight-power scaling of the propulsors predict with DP.

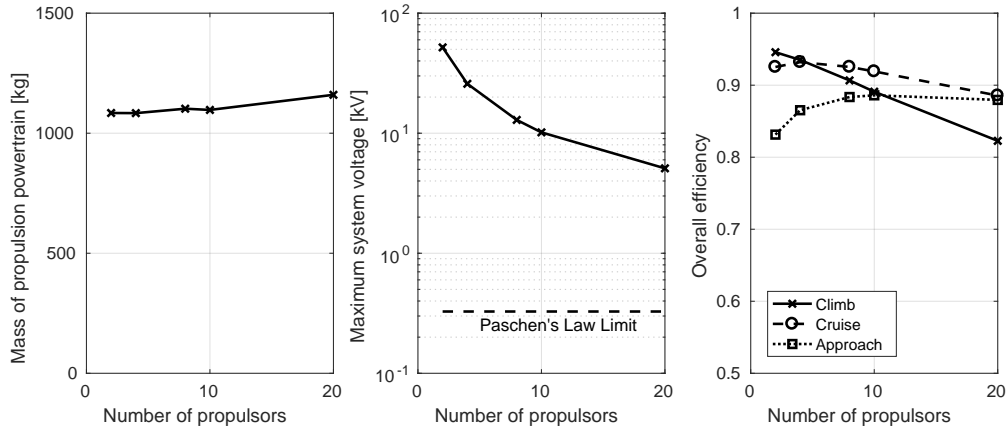


Fig. 13 Effects of distributed propulsion.

E. Limitations and Future Work

The higher-fidelity models and the integrated system presented in this work have a number of limitations. The first involves drawing the control volume boundary at the end of the powertrain, instead of incorporating the propulsors and modeling the entire propulsion system. Neglecting the propulsor mass fails to capture the weight saving benefits of distributed propulsion, and does not provide a complete estimate of the overall propulsion system mass. The propulsion system also needs to account for thermal management, to deal with the energy lost as heat due to the inefficiencies of the motor and converter. For specific aircraft configurations, the wiring system (mass and losses) also need to be modeled. Future work will incorporate a propulsor model, as well as develop thermal management and wiring models.

In addition, the inability of the motor model to size motors for currents higher than 150 A means the system voltages are much higher than what Paschen's law allows. This suggests that the power distribution system is important—protective measures to develop flight-safe high-voltage, high-current systems and components need to be considered. Alternatively, or in addition, the motor sizing technique needs to be modified to handle higher current levels, possibly moving towards the use of lamination materials with different magnetic characteristics.

While this work captures operational behavior of the powertrain components, it still sizes their masses based on specific energy and specific power. A mass buildup and/or a volume buildup would provide a more accurate picture. Parts for the mass buildup of the motor already exist in terms of calculating the core losses. Future work will extend this to the whole machine.

Finally, this work only considers the propulsion powertrain, which fails to capture benefits associated with electrification. The aircraft as a whole needs to be looked at, which means modeling enabling and beneficial aspects like distributed propulsion as mentioned, and boundary layer ingestion (BLI) at system level. Due to the much low battery specific energy (BSE) compared to that of fuel, hybrid-electric and turbo-electric architectures are likely to be better than all-electric systems for larger sizes and longer missions [2, 3]. Therefore, future work will extend the powertrain to handle hybrid- and turbo-electric architectures as well, with the goal of eventually integrating the power systems into a full aircraft modeling framework.

V. Summary and Conclusions

This paper presents models for the three major components of an all-electric propulsion system (motor, converter, battery), as well as a method to integrate the components into a powertrain. The models capture operational behavior under variable power loads as required to represent the different flight segments, without diving into minute details about component materials and battery chemistry. The powertrain is designed so that alternative or updated models of its components can be substituted as necessary, making it a modular framework to model all-electric propulsion.

Results show that the higher-fidelity model consistently predicts higher energy requirements than low-fidelity modeling approaches, resulting in a larger battery and heavier powertrain. In particular, the high climb power requires the battery to be sized based on power given the reduction in battery efficiency with power level, leading to a higher

energy usage during climb than during the significantly longer cruise segment for a commuter aircraft.

The efficiencies of the motor and the converter change when run at power levels different from those they were designed for. For lower-power operations, the motor efficiency goes down due to the relatively constant core losses forming a higher proportion of the total power lost. The converter efficiency goes up at lower power due to the lower copper losses, which are more important than the constant switching losses. Distributed propulsion helps increase the efficiency of the system at lower power, where the motor efficiency goes up without sacrificing a lot in converter efficiency. The high voltages and currents that result from this analysis call for a rethinking of the power distribution system to handle high voltages and high currents beyond those available today in order to enable power system electrification.

References

- [1] Moore, M. D., and Fredericks, B., “Misconceptions of electric propulsion aircraft and their emergent aviation markets,” AIAA 2014-0535, 2014 AIAA SciTech, National Harbour, MD, 13–17 Jan., 2014. doi:10.2514/6.2014-0525.
- [2] Kruger, M., Byahut, S., Uranga, A., Dowdle, A., Gonzalez, J., and Hall, D. K., “Electrified Aircraft Trade-Space Exploration,” AIAA 2018-4227, 2018 AIAA Aviation, Atlanta, GA, 25–29 June, 2018. doi:10.2514/6.2018-4227.
- [3] Hall, D., Greitzer, E., Dowdle, A., Gonzalez, J., Hoburg, W., Lang, J., Sabnis, J., Spakovszky, Z., Yutko, B., Courtin, C., Thalheimer, W., Trollinger, L., Tylko, J., Varney, N., Uranga, A., Byahut, S., and Kruger, M., “Feasibility of Electrified Propulsion for Ultra-Efficient Commercial Aircraft, Final Report,” NASA CR to appear, 2018.
- [4] Kuhn, H., and Sizmann, A., *Fundamental prerequisites for electric flying*, Deutsche Gesellschaft für Luft-und Raumfahrt-Lilienthal-Oberth eV, 2012.
- [5] German, B. J., “Introduction to Batteries and Cell Discharge Modeling for Electric Aircraft Design,” Lecture and Presentation at AIAA Workshop on Electric Aircraft Design, June, 2018.
- [6] NASA, “Scalable Convergent Electric Propulsion Technology and Operations Research (SCEPTOR) Critical Design Review Day 1 Package,” https://www.nasa.gov/sites/default/files/atoms/files/sceptor_cdr_day_1_package.pdf, 2016.
- [7] Krishnan, R., *Switched Reluctance Motor Drives*, CRC Press, 2001.
- [8] Bradley, M., and Dorney, C., “Subsonic Ultra Green Aircraft Research: Phase II – Volume II – Hybrid Electric Design Exploration,” 2015.
- [9] Kisner, R. A., Melin, A. M., Drira, A., Reed, F. K., and Fugate, D., “Embedded Sensors and Controls to Improve Component Performance and Reliability – Bench-scale Testbed Design Report,” 2015. doi:10.13140/RG.2.1.2554.9525.
- [10] Torrent, M., Andrada, P., Blanque, B., Martinez, E., Perat, J. I., and Sanchez, J. A., “Method for estimating core losses in switched reluctance motors,” *European Transactions on Electrical Power*, 2010. doi:10.1002/etep.475.
- [11] Erickson, R. W., and Maksimovic, D., *Fundamentals of Power Electronics, Second Edition*, Kluwer Academic Publishers, 2004.
- [12] Sundaresan, S., Sturdevant, C., Mairipelly, M., Lieser, E., and Singh, R., “12.9 kV SiC PiN diodes with Low On-state Drops and High Carrier Lifetimes,” *Materials Science Forum*, Vol. 717-720, 2012.
- [13] Zhang, Q., Das, M., Sumakeris, J., Callanan, R., and Agarwal, A., “12-kV p-Channel IGBTs with Low On-Resistance in 4H-SiC,” *IEEE Electron Device Letters*, Vol. 29, No. 9, 2008.
- [14] Airbus Group, “E-Fan The New Way to Fly,” <http://www.airbusgroup.com/service/mediacenter/download/uuid=48b1bd2c-a428-4c65-82e5-ed3e923bd142>, 2015. Accessed: 07/26/2016.
- [15] The National Academies of Sciences, Engineering, and Medicine, “Commercial Aircraft Propulsion and Energy Systems Research: Reducing Global Carbon Emissions,” 2016.
- [16] Jansen, R. H., Bowman, C., Jankovsky, A., Dyson, R., and Felder, J., “Overview of NASA Electrified Aircraft Propulsion Research for Large Subsonic Transports,” *53rd AIAA/SAE/ASEE Joint Propulsion Conference*, 2017.
- [17] Viking Air Ltd., “Viking Twin Otter Series 400 Technical Specifications and Standard Equipment List,” 2016.
- [18] Gibbs, Y., and NASA, “NASA Armstrong Fact Sheet: NASA X-57 Maxwell,” <https://www.nasa.gov/centers/armstrong/news/FactSheets/FS-109.html>, 2017. Accessed: 05/07/2018.

- [19] Raymer, D. P., *Aircraft Design: A Conceptual Approach (AIAA Education Series) 5th Edition*, American Institute of Aeronautics and Astronautics (AIAA), 2012.
- [20] Clarke, S., "SCEPTOR Power System Design: Experimental Electric Propulsion System Design and Qualification for Crewed Flight Testing (Presentation)," , 2016.